Arch. Metall. Mater. **69** (2024), 4, 1323-1332

DOI: https://doi.org/10.24425/amm.2024.151395

NIANCHU WU[1*], TINGTING LI[1], XIAOTIAN SU[1]

# THE EFFECT OF BARREL CONFIGURATIONS ON THE POROSITY DURING HVAF THERMAL SPRAY Ni-BASED AMORPHOUS COATINGS: NUMERICAL SIMULATION AND EXPERIMENT

The relationship between barrel configurations and porosity of a Ni-based amorphous coating (AM) that is fabricated using a high-velocity air fuel (HVAF) process was revealed by both numerical and experimental methods. A computational fluid dynamics model was applied to investigate the gas-flow field and the behavior of in-flight particles with various barrel configurations. It is found that barrel length obviously affects the particle velocity and temperature while it has a slight influence on the particle velocity and temperature. The longer the barrel length (diameter), the higher the flame (particle) velocity and temperature. By analyzing both particle velocity and temperature, the optimal barrel configuration (4E) to achieve low-porosity coatings was predicted. These calculations were experimentally verified by the production of a low-porosity (2.09%) Ni-based AM that was fabricated by HVAF using the predicted optimal barrel configuration.

*Keywords:* Ni-based amorphous coating; porosity; HVAF; computational simulation; barrel configuration

## Notation

$A_p$ – surface area of the particle
$C_D$ – drag coefficient
$c_p$ – specific heat of the particle
$d_p$ – particle diameter
$E$ – enthalpy
$F_x$ – additional acceleration
$h$ – heat transfer coefficient
$k$ – thermal conductivity
$k_{eff}$ – effective thermal conductivity
$m_p$ – mass of the particle
$p$ – pressure
$Re$ – Reynolds number
$S_h$ – chemical reaction source energy
$T$ – temperature
$T_g$ – gas temperature
$T_p$ – particle temperature
$u$ – velocity
$u_i$ – velocity in the i-direction
$u_p$ – particle velocity
$x_i$ – coordinate in the i direction
$A$ – constant in eddy dissipation model = 4.0
$B$ – constant in eddy dissipation model = 0.5
$k$ – kinetic energy, $m^2/s^2$
$M_{w,i}$ – molecular weight of species $i$
$M_{\omega,R}$ – molecular weight of reactant $R$
$M_{\omega,j}$ – molecular weight of reactant $j$
$N$ – number of chemical species in the system
$p$ – pressure, Pa
$R_{i,r}$ – net rate of production of species $i$ due to reaction $r$
$v_{i,r}$ – stoichiometric coefficient for reactant $i$ in reaction $r$
$Y_P$ – mass fraction of product $P$
$Y_R$ – mass fraction of a particular reactant, $R$

### Greek letters

$\delta$ – Kronecker symbol
$\mu$ – viscosity
$\mu_t$ – turbulent viscosity
$\rho$ – density
$\tau$ – deviatoric stress tensor

### Subscripts

$g$ – gas
$i, j$ – coordinate indices
$p$ – particle
$\varepsilon$ – turbulence dissipation rate, $m^2/s^3$
$\rho$ – density, $kg/m^3$

[1] LIAONING PETROCHEMICAL UNIVERSITY, SCHOOL OF MECHANICAL ENGINEERING, FUSHUN, 113001, P.R. CHINA

* Corresponding author: wunianchu@163.com

## 1. Introduction

Ni-based amorphous alloys exhibited ultrahigh strength and high thermal stability owing to their high glass transition temperature as well as excellent corrosion resistance [1]. In most cases, the Ni-based amorphous alloys were prepared in the form of ribbons, powders and wires of small thickness or diameter. Therefore, the application of amorphous alloys as a structural material has been limited by glass forming ability. However, amorphous coatings based on Ni-based metallic glasses systems prepared via different methods on substrates can overcome the drawback.

Nowadays, there are several methods used to produce amorphous coatings, such as the laser cladding and thermal spray-based techniques. It has been reported that Ni-based amorphous coatings (AMs) were successfully coated into metallic components and that these coatings exhibit optimised corrosion resistance compared to the properties of the crystalline substrates [2,3]. In Laser cladding, the coating is usually a composite structure composed of amorphous, nanocrystalline and metal compound phases [4]. They failed to obtain an amorphous coating and the absence of an amorphous structure could be explained as [5]: (1) the redistribution of elements in weld metal; (2) devitrification resulted from the reheating cycles induced by the successive laser tracks; (3) epitaxial solidification which favors the crystal growth; (4) inter-diffusion or dilution of some phases of substrate in the layer. In addition, partial amorphous metallic coatings in Ni-based alloy systems have been fabricated currently by plasma spraying and high velocity oxygen fuel (HVOF) spraying techniques [6,7]. HVAF is a similar spraying process as HVOF, just using air to replace oxygen. Considering that a high particle velocity is expected to produce a dense coating [8], HVAF is a good candidate to deposit Ni-based amorphous alloy coating. However, a fully amorphous Ni-based coating is difficult to be achieved by HVAF so far.

Porosity is one of the most important quality parameters for coatings produced by the thermal spray because porosity considerably influences the mechanical, chemical, and magnetic properties; the thermal conductivity; and the electrical conductivity of the coated materials [9,10]. The porosity of HVOF sprayed coatings is strongly influenced by the structure of the deposit, which largely depends on the particles velocity and temperature during the point of impact on the substrate [11,12]. In HVAF spray process, the particles' velocity and temperature can be efficiently controlled by changing process parameters [13]. As we all know, the barrel section is a cylindrical tube that has the same diameter of the nozzle exit. Coating particles are injected in this section to be melted or semi-melted and then form the coating layer onto a substrate. This barrel section is responsible for controlling and optimizing the coating porosity by adjusting particles' velocity and temperature. Nevertheless, the optimal length for this section should be tested in a set of variable lengths. Barrel optimization work usually relies on cost intensive trial and error procedures. This approach is expensive but reliable for thermal spray process. Numerical computational fluid dynamics (CFD) simulations have been used to investigate the effect of nozzle geometry and Air/Fuel ratio on the flame flow characteristics and particle flight characteristics [14]. However, systematic study about the effect of barrel on the porosity of the HVAF sprayed Ni-based AMs is still very rare. Therefore, it is important to combine the CFD simulations with experiment to study the relationship between barrel and the coating porosity during HVAF sprayed Ni-based AMs.

In the paper, the $Ni_{53}Nb_{20}Ti_{10}Zr_8Co_6Cu_3$ (at. %) amorphous alloy is selected as the thermally-sprayed material because of its excellent glass forming ability [15]. The effect of barrel size on the characteristics of flame flows and in-flight Ni-based amorphous particles during spraying was studied by CFD simulations. Using the optimal barrel that was predicted via simulation, a Ni-based AM with a low porosity was fabricated by the HVAF thermal spray process.

## 2. Mathematical modeling

### 2.1. HVAF thermal spray gun model and boundary

Fig. 1 shows the detailed mesh of the AK06 spray gun. The numerical methods and mathematical models are applied to a propane-fueled 2-D geometry. There are a total of 82,331 cells and 83,235 nodes in the whole domain. The free jet region, the air-fuel inlet, and the grids around the nozzle have been successively refined to accurately capture the characteristics of the flame flow. TABLE 1 shows the spray parameters for HVAF sprayed Ni-based AMs. And 6 different barrel configurations (3L, 3E, 4L, 4E, 5L, 5E) were shown in TABLE 2. Barrel length and barrel diameter are two key points for the barrel configuration. There are 12 mm and 14 mm for the barrel exit diameter,

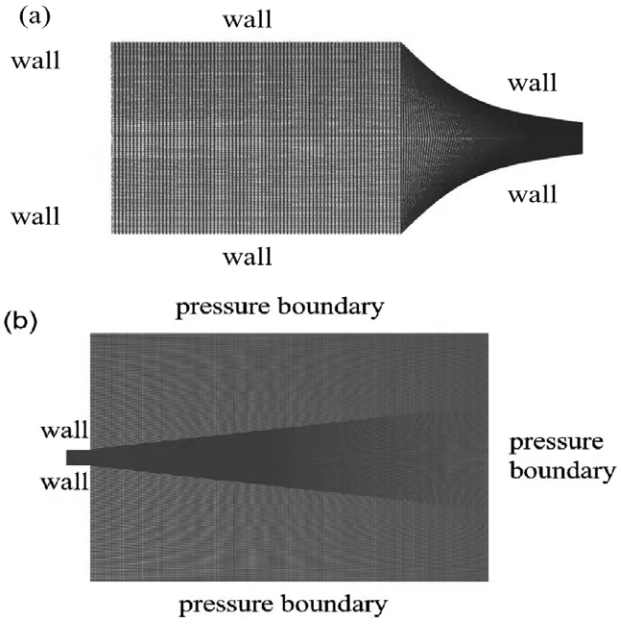


Fig. 1. Computational grid and boundary conditions used in the HVAF model. (a) The internal domain, including the combustion chamber and the convergent-divergent nozzle. (b) External domain

which named E and L, respectively. And there are 210 mm, 230 mm and 280 mm for the barrel length, which named 3, 4 and 5, respectively. The powder particles are introduced downstream of the nozzle using a carrier gas [16]. Particles in the size-range between 10 μm and 50 μm are injected into the nozzle. The walls of the spray gun are all assumed to be at a constant temperature of 300 K. The pressure far field and pressure outlet boundary is applied at the external domain. Finally, the atmospheric pressure is assumed to be 1.01 KPa.

TABLE 1

HVAF spray parameters for Ni-based AMs

| Air pressure (Psi) | Propane pressure (Psi) | nitrogen pressure (Psi) | chamber pressure (Psi) | Feed rate (g/min) | Traverse velocity (mm/s) | Spray distance (mm) |
|---|---|---|---|---|---|---|
| 90.4 | 94.8 | 76.0 | 74.3 | 30 | 500 | 350 |

TABLE 2

Different barrel configurations (3L, 3E, 4L, 4E, 5L, 5E) f or HVAF thermal spray Ni-based AMs. There are 12 mm and 14 mm for the barrel exit diameter, which named E and L, respectively. And there are 210 mm, 230 mm and 280 mm for the barrel length, which named 3, 4 and 5, respectively

| Barrel | 3L | 3E | 4L | 4E | 5L | 5E |
|---|---|---|---|---|---|---|
| Barrel length (mm) | 210 | 210 | 230 | 230 | 280 | 280 |
| Barrel diameter (mm) | 12 | 14 | 12 | 14 | 12 | 14 |

### 2.2. Gas flow model

The "realizable $k$-$\varepsilon$ model" is used extensively in the HVAF simulation. The governing equations for the 2-D model in the Cartesian tensor are defined below [17]: Mass conservation equation:

$$\frac{\partial \rho}{\partial t}+\frac{\partial}{\partial x_i}\left(\rho u_i\right)=0 \tag{1}$$

Momentum conservation:

$$\frac{\partial}{\partial t}\left(\rho u_i\right)+\frac{\partial}{\partial x_j}\left(\rho u_i u_j\right)= =-\frac{\partial p}{\partial x_i}+\frac{\partial}{\partial x_j}\left(\tau_{ij}\right)_{eff}+\frac{\partial}{\partial x_j}\left(-\rho \overrightarrow{u_i' u_j'}\right) \tag{2}$$

Energy transport equation:

$$\frac{\partial}{\partial t}\left(\rho E\right)+\frac{\partial}{\partial x_i}\left[u_i\left(\rho E+p\right)\right]= =\frac{\partial}{\partial x_j}\left(k_{eff}\frac{\partial T}{\partial x_j}+u_i\left(\tau_{ij}\right)_{eff}\right)+S_h \tag{3}$$

$$\left(\tau_{ij}\right)_{eff}=\mu_{eff}\left(\frac{\partial u_j}{\partial x_i}+\frac{\partial u_i}{\partial x_j}\right)-\frac{2}{3}\mu_{eff}\frac{\partial u_i}{\partial x_i}\delta_{ij} \tag{4}$$

Whereas the effective thermal conductivity is

$$k_{eff}=k+\frac{c_p\mu_t}{\sigma_t} \tag{5}$$

### 2.3. Combustion model

In practice, the chemical reactions between hydrocarbon and air in the HVAF chamber are extremely complex, not only because they consist of a large number of elementary reactions, but also because the combustion products may decompose at high temperature and pressure due to the strong thermal vibration of atoms [18]. Therefore, it is necessary to simplify the chemical reactions in the combustion chamber. In this study, the chemical equilibrium code developed by Gorden and McBride [19] is used to calculate the stoichiometry of each product. The chemical reaction considered in our model is as follows:

$$\begin{aligned}&C_3H_8+4.762O_2+0.014N_2\rightarrow 0.447CO\\&+2.553CO_2+0.009H+0.129H_2+3.843H_2O\\&+0.027NO+0.002O+0.047OH+0.026O_2\end{aligned}$$

An eddy dissipation model is used to solve this global reaction. This approach is based on the solution of transport equations for species mass fractions. The reaction rates are assumed to be controlled by the turbulence rather than a calculation of the Arrhenius chemical kinetics. The net rate of production for species $i$ due to reaction $r$, is given by the smaller of the two equations below:

$$R_{i,r}=\upsilon_{i,r}M_{w,i}A\rho\frac{\varepsilon}{k}\min\left(\frac{Y_R}{\upsilon_{R,r}M_{\omega,R}}\right) \tag{6}$$

$$R_{i,r}=\upsilon_{i,r}M_{w,i}AB\rho\frac{\varepsilon}{k}\left(\frac{\sum_P Y_P}{\sum_j^N \upsilon_{j,r}M_{\omega,j}}\right) \tag{7}$$

### 2.4. Particle models

The gas is treated as a continuum phase by solving the Navier-Stokes equations, while the dispersed particle phase is solved by tracking a large number of droplets. The trajectories of these discrete phase entities are computed, in addition to the heat and mass transfer to the gas phase.

The equation of motion for particles in the $x$ direction (using Cartesian coordinates) can be written as a force balance that equates the droplet inertia with forces acting on the particle. The basic equations for a particle are as follows [16].

$$\frac{du_p}{dt}=\frac{18\mu}{\rho_p d_p^2}\frac{C_D\,\mathrm{Re}}{24}\left(u-u_p\right)+F_x \tag{8}$$

The energy equation for a single particle, neglecting the heat transfer via radiation, is given by [20]:

$$m_p c_p \frac{dT_p}{dt} = hA_p \left(T_g - T_p\right) \tag{9}$$

where the density of the Ni-based amorphous alloy is 8200 kg/m$^3$ and the specific heat is 400 J/(kg·K).

## 3. Experimental procedures

The material used in this work is a $Ni_{53}Nb_{20}Ti_{10}Zr_8Co_6Cu_3$ (at. %) alloy. The master alloy with the above nominal composition was prepared by arc-melting appropriate amounts of high-purity elemental constituents in a water-cooled copper crucible under a Ti-gettered argon atmosphere. The amorphous ribbons were fabricated using a Bühler melt spinner (Hechingen, Germany) and the copper wheel rotating was speed of 40 m/s. The amorphous powders (–10+50 μm) were prepared by high-purity argon gas atomization at a dynamic pressure of 7 MPa after heating up to approximately 1473 K using a close-coupled annulus nozzle. The atomized powders were sieved according to conventional sieve analysis and divided into different size ranges. A type 304 stainless steel plate with dimensions of 100 mm×40 mm×5 mm was selected as the substrate. The $Ni_{53}Nb_{20}Ti_{10}Zr_8Co_6Cu_3$ AM was fabricated using an AK06 HVAF thermal spray system by Kermetico company. The detailed spraying parameters for the HVAF process are shown in the TABLE 1.

The microstructure of the powders and coatings was examined by SEM (Quanta 600). X-ray diffraction (XRD) analysis of the ribbon and coatings was conducted on a Rigaku D/max 2400 diffractometer (Tokyo, Japan) with monochromated Cu $K_\alpha$ radiation ($k$ = 0.1542 nm). Image analysis techniques have become popular for determining porosity in thermal spray coatings because of their simplicity, accessibility, and ability to measure porosity [21]. Porosity can be easily detected in the SEM micrographs by image analysis due to the high degree of contrast between the dark pores and the more highly reflective coating material. Porosity was evaluated by analyzing SEM micrographs with Image-Pro-Plus 6.0 software. Twenty fields of random, non-overlapping SEM images were taken for each sample. All the images were taken with the same acceleration voltage, working distance, resolution, and magnification.

## 4. Results and discussion

### 4.1. Gas dynamics for different barrel configurations

Fig. 2, Fig. 3 and Fig. 4 show the predicted contours of pressure, and gas velocity, gas temperature of the flame along the centerline for different barrel configurations (3L, 3E, 4L, 4E, 5L, 5E). In order to investigate the effect of barrel length and barrel diameter on the gas flow characteristics, the distribution of pressure, and gas velocity, gas temperature at the centerline of HVAF thermal spray gun are shown in Fig. 5 and Fig. 6. The air and propane are injected into a combustion chamber and undergo a chemical reaction that converts them to a high temperature and pressure gas. The high-pressure gas flows through the constrained nozzle, giving rise to a supersonic flame flow. The gas pressure is approximately 7 KPa in the combustion chamber and below 1.0 KPa in the barrel, but the pressure fluctuates in the vicinity of the gun exit, as shown in Fig. 5a,b and Fig. 6a-c. The fluctuations in the flame pressure at the barrel exit are created by the flow periodically over-expanding and subsequently re-converging above and below atmospheric pressure [22]. In the atmospheric environment, the flame flow pressure curve undergoes a sudden zigzag change and the amplitude decreases, then remaining at the standard atmospheric pressure level. When the flame flow hits the substrate, the surface of the substrate

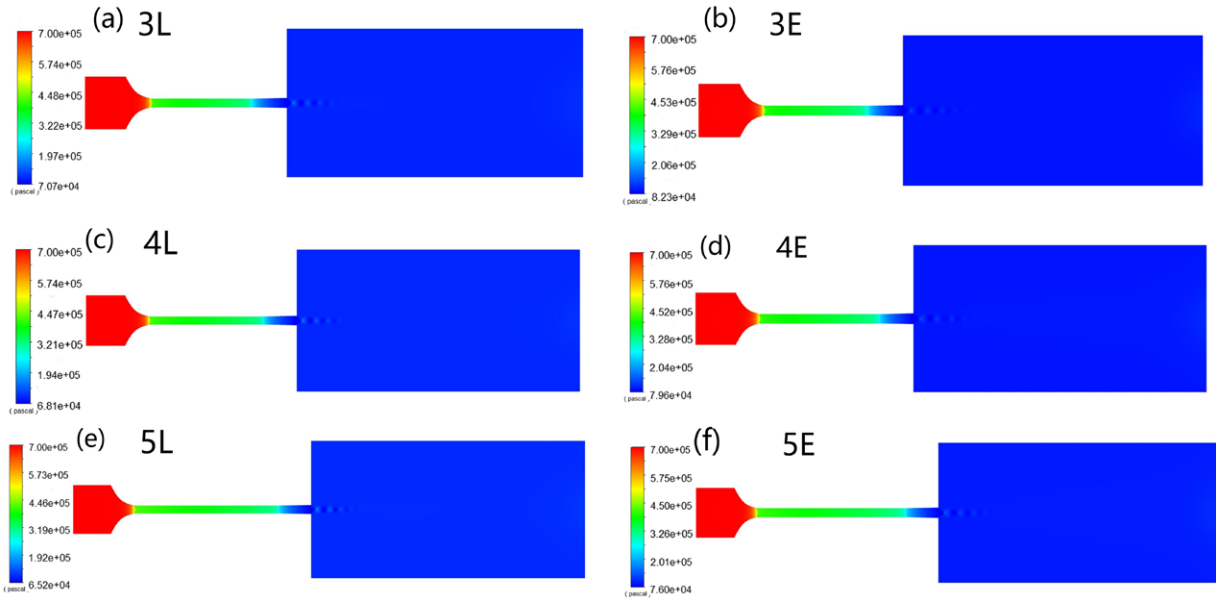


Fig. 2. Contours of gas pressure for different barrel configurations (3L, 3E, 4L, 4E, 5L, 5E)

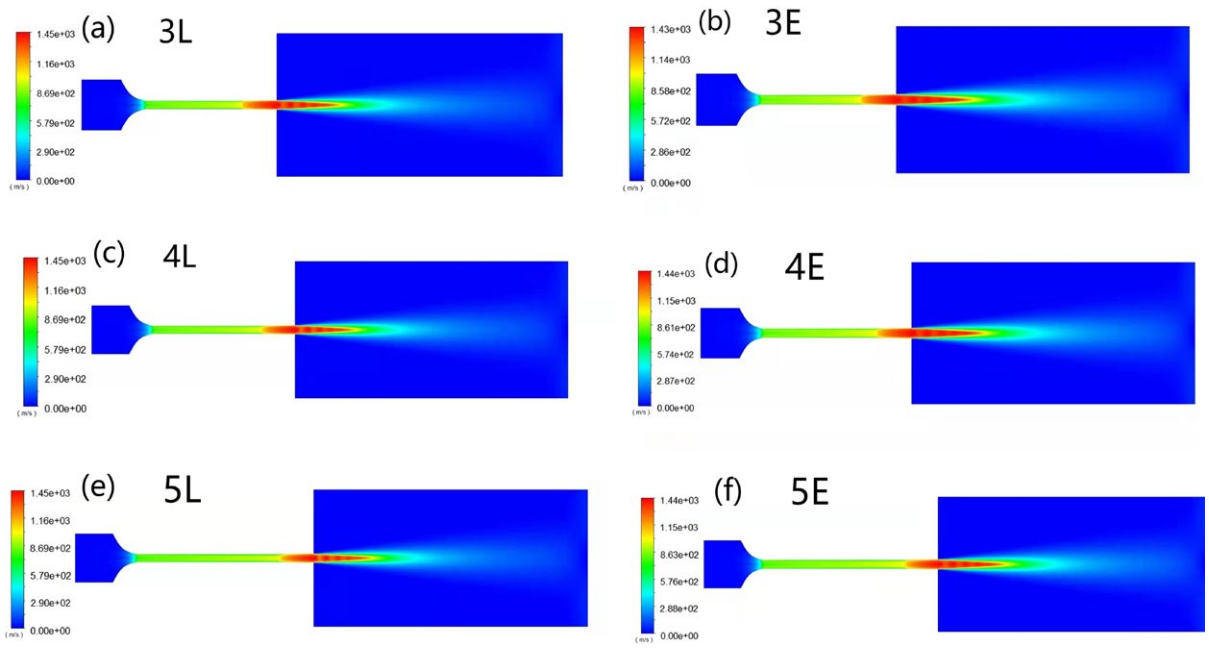


Fig. 3. Contours of gas velocity magnitude for different barrel configurations (3L, 3E, 4L, 4E, 5L, 5E)

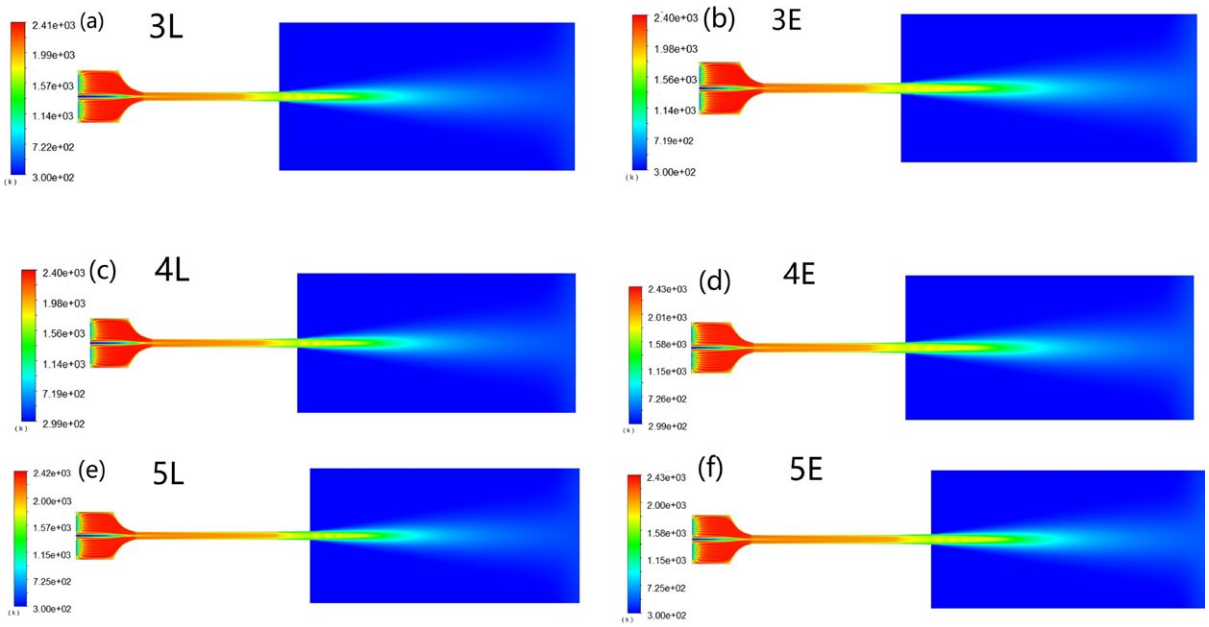


Fig. 4. Contours of gas temperature for different barrel configurations (3L, 3E, 4L, 4E, 5L, 5E)

forms an inverted small arched shock wave. Fig. 3 shows that the combustion chamber's flame flow velocity is about 10 m/s and the velocity increases gradually in the CD nozzle and barrel. Five diamond waves appear at the nozzle exit, which then gradually decays until it disappears. Due to the impact of the shock wave, the flame flow velocity increased to 1462 m/s, and the velocity curve fluctuated with decreasing amplitude. When the momentum is exhausted, the flame flow velocity drops sharply to 0 m/s. Fig. 4 shows that the gas temperature increases sharply within the combustion nozzle and barrel and reaches its peak near the exit of the nozzle. The higher centerline temperature is about 1950 K. There are five noticeable hollow circles in the core of the free jet. The temperature curve shows damping oscillation.

As shown in the Fig. 5a,b and Fig. 6a-c, the barrel diameter and barrel length have no effect on the initial chamber pressure. As the barrel length is increased (see Fig. 5a,b), the location of Mach shock disc moves backward from the nozzle exit. There are shock waves of equal magnitude at the barrel outlet as increasing the barrel length. But shock waves of magnitude at the barrel outlet in the distribution of pressure increases with increasing the barrel diameter and these changes result in the severe fluctuation of flame velocity and temperature at the barrel exit. Changing the HVAF barrel length from 210 mm to 280 mm or barrel diameter from 12 mm to 14 mm increased both the flame velocity and temperature (see Fig. 5c-f and Fig. 6d-i).

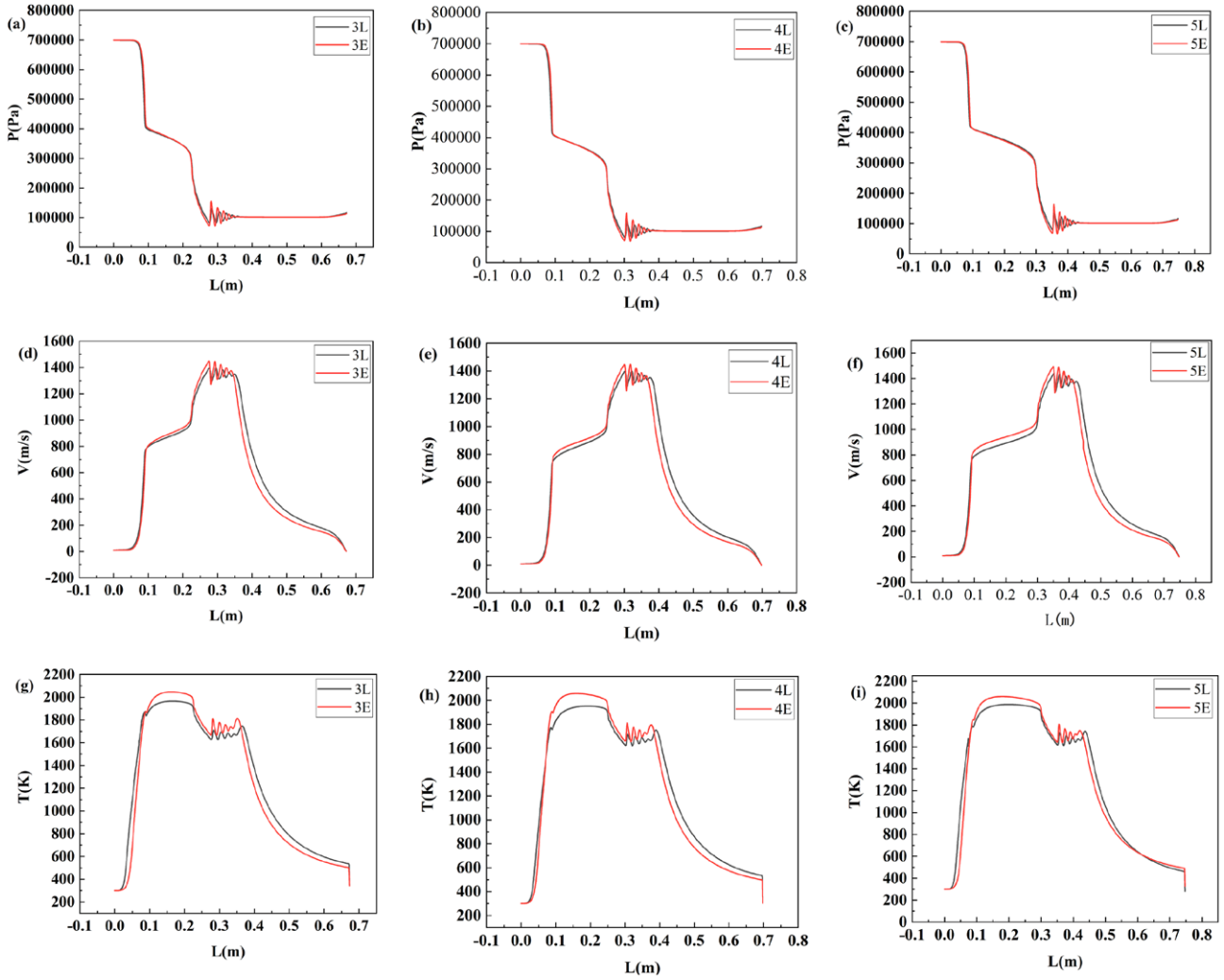


Fig. 5. Calculated contours of the flame and gas characteristics along the centerline (a) (b) gas pressure (Pa), (c) (d) gas temperature (K), (e) (f) gas velocity magnitude (m/s) for different barrel lengths (3, 4, 5)

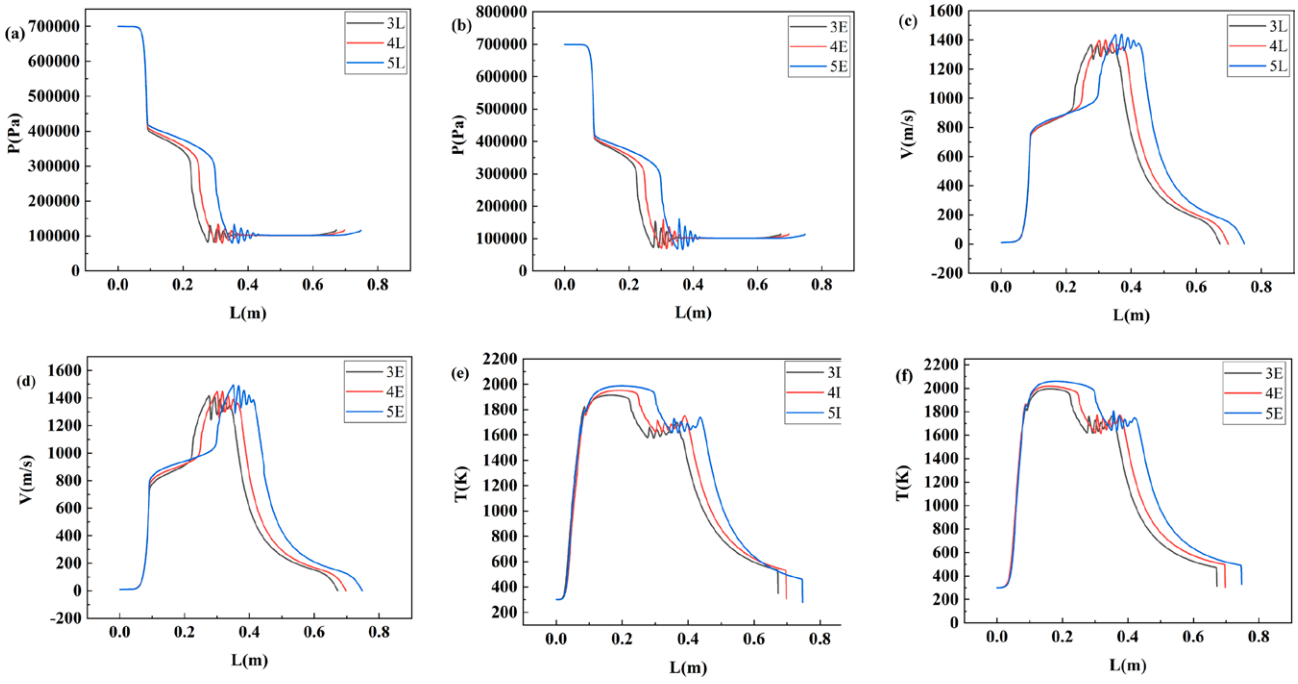


Fig. 6. Calculated contours of the flame and gas characteristics along the centerline (a) (b) (c) gas pressure (Pa), (d) (e) (f) gas temperature (K), (g) (h) (i) gas velocity magnitude (m/s) for different barrel diameters (L, E)

### 4.2. Effect of the barrel configurations on particle velocity and temperature

Fig. 7 shows the particle velocity and temperature curves along the centerline with different barrel lengths (3, 4 and 5) for the same particle size (10-50 μm). In this experiment, particle size has a strong effect on the particle acceleration and deceleration behavior. Small particles can be heated to the melting point in a short time and they might eventually be in a coexistence state of liquid and solid or even full solid-state after a long enough distance. Smaller particles tend to change their temperatures relatively easily due to their smaller thermal inertias. For large particles, the periods for acceleration and heating are both longer, and their temperature profiles become nearly flat. As shown in Fig. 7a,b, when the barrel length increases from 210 mm to 280 mm (from 3 to 5), the particle (e.g. 30 μm) impact velocity increases by 16% and the particle temperature increases by 14% because the particles stay in the flame flow for a longer time to gain more heat. Fig. 8 represents the particle velocity and temperature as a function of the distance along the centerline for different barrel

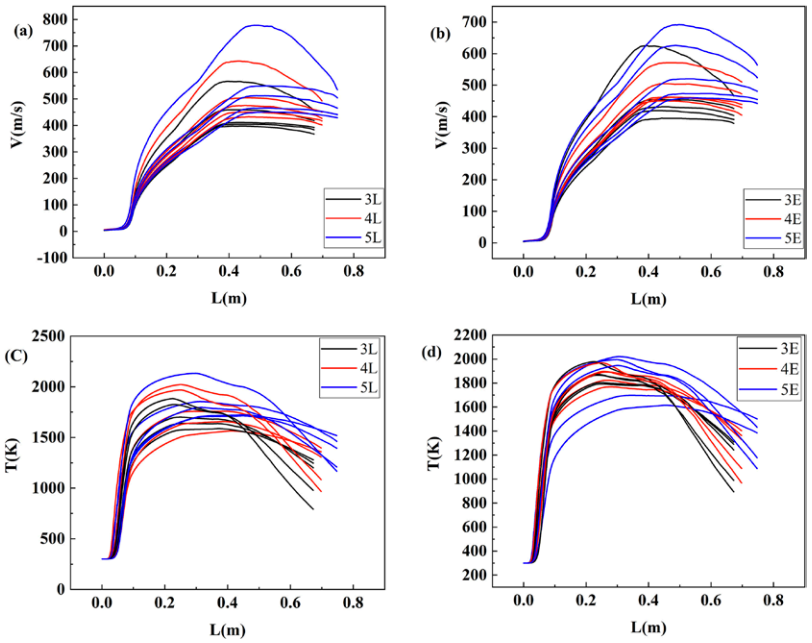


Fig. 7. Calculated contours of the in-flight particle characteristics along the centerline (a) (b) gas velocity magnitude (m/s) and (c) (d) gas temperature (K) for different barrel lengths (3, 4, 5)

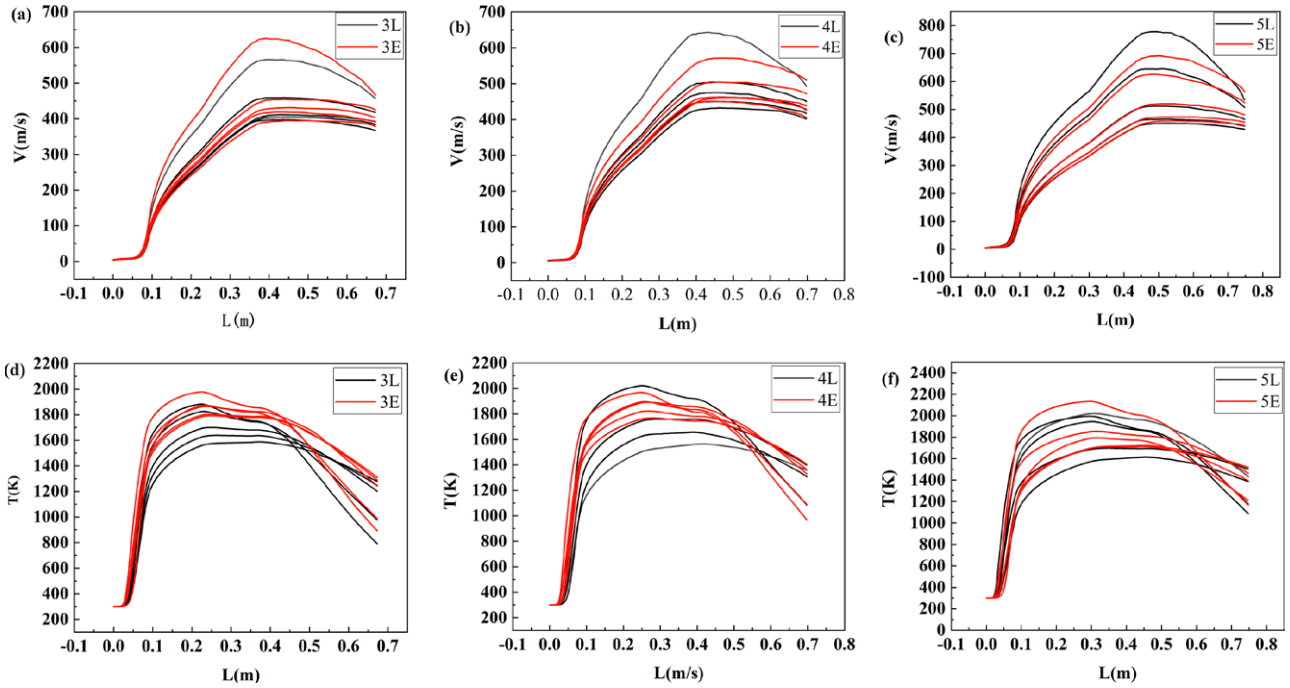


Fig. 8. Calculated contours of the in-flight particle characteristics along the centerline (a) (b) (c) gas velocity magnitude (m/s) and (d) (e) (f) gas temperature (K) for different barrel diameters (L, E)

diameter (L and E) for the same particle size (10-50 μm). Comparing with barrel length, the change of barrel diameter has a weaker effect on the particle velocity and temperature. Therefore, the particle velocity and temperature impacting the substrate can be adjusted by changing the barrel length and barrel diameter.

Fig. 9 shows the particle velocity and temperature impact the substrate with different barrel configurations (3L, 3E, 4L, 4E, 5L, 5E) for the same particle size (10-50 μm). It can be seen that the axial particle velocity and temperature at impact all increase with barrel length and barrel diameter for particle size from 10 μm to 50 μm. The particle velocity and temperature at impact for barrel configuration 5E is the highest than other barrel size (3L, 3E, 4L, 4E, 5L). Particle velocity and temperature are the most significant factors in determining the porosity of a HVAF coating [23,24]. Increased particle velocity generally correlates with improved splat deformation but has a weak effect on porosity. Particle temperature determines the melting behavior of the particles and is the key to creating low porosity, dense coatings [11]. The optimum thermal spraying occurs when the temperature of the powder is between the solidus and liquidus temperatures ($T_m$ and $T_L$) of the Ni-based amorphous material [25]. Barrel 4E and 4L might be mostly melted during flight because their temperature is between $T_m$ = 1302 K and $T_L$ = 1338 K (see Fig. 9a). As we all known that the increase in particle velocity significantly improved the coating density. As show in the Fig. 9b, the particle velocity at impact for barrel size 4E is larger than the particle velocity at impact for barrel size 4L. Thus we found that the optimal barrel configuration is 4E for the Ni-based AMs.

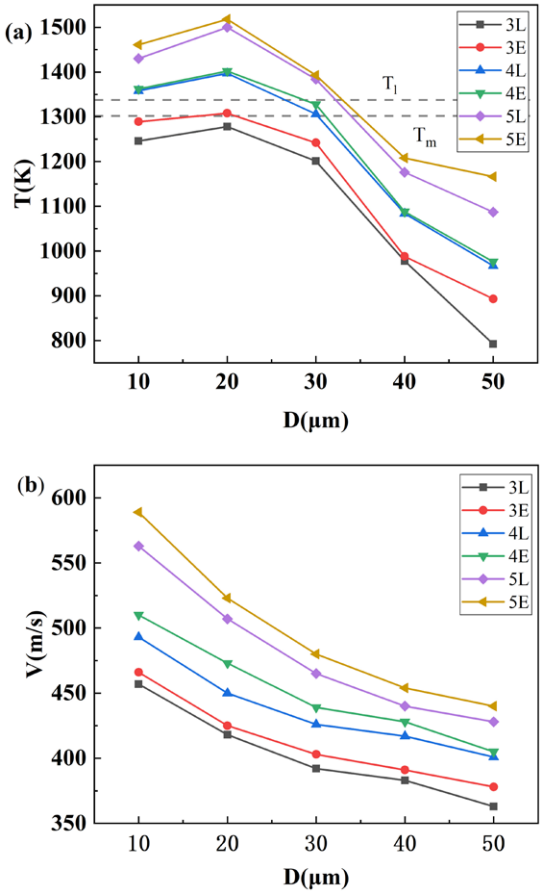


Fig. 9. Predicted particle axial velocity (a) and temperature (b) at a spray distance of 350 mm for particle size from 10 μm to 50 μm and different barrel configurations (3L, 3E, 4L, 4E, 5L, 5E)

### 4.3. Experimental validation

To validate the simulations, Ni-based AMs were fabricated by using powders with four barrel configurations (3L, 3E, 4L, 4E, 5L, 5E). Fig. 10 shows SEM images of the $Ni_{53}Nb_{20}Ti_{10}Zr_8Co_6Cu_3$ feedstock powders. The majority of the particles that were produced by gas atomization in the argon atmosphere were spherical or near-spherical. Although some particles had small satellites attached, most of them showed smooth surfaces, which correspond to good fluidity. The XRD patterns of the atomized powders, $Ni_{53}Nb_{20}Ti_{10}Zr_8Co_6Cu_3$ melt-spun ribbon and the as-deposited coatings for each barrel size (3E, 4L, 4E, 5L) are shown in Fig. 11. The diffuse pattern and the absence of any

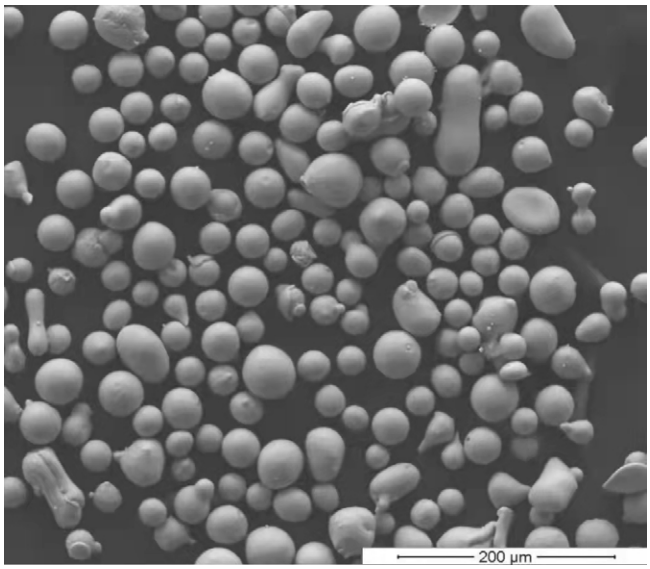


Fig. 10. SEM image of $Ni_{53}Nb_{20}Ti_{10}Zr_8Co_6Cu_3$ alloy powders

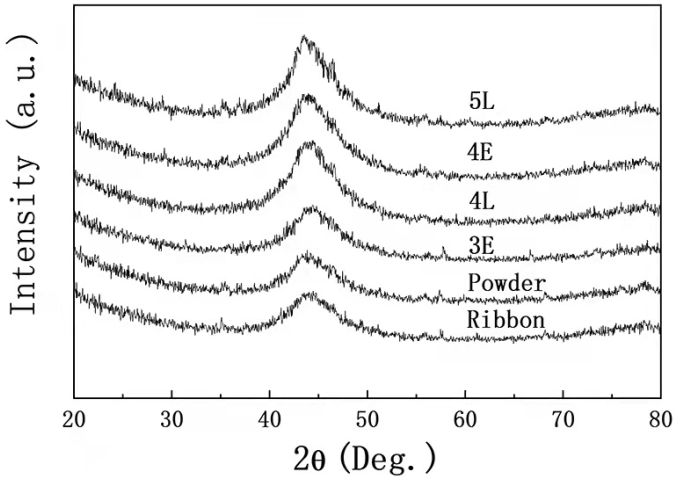


Fig. 11. XRD patterns for the $Ni_{53}Nb_{20}Ti_{10}Zr_8Co_6Cu_3$ melt-spun ribbons, atomized powders and HVAF sprayed AMs using different barrel configurations (3E, 4L, 4E, 5L)

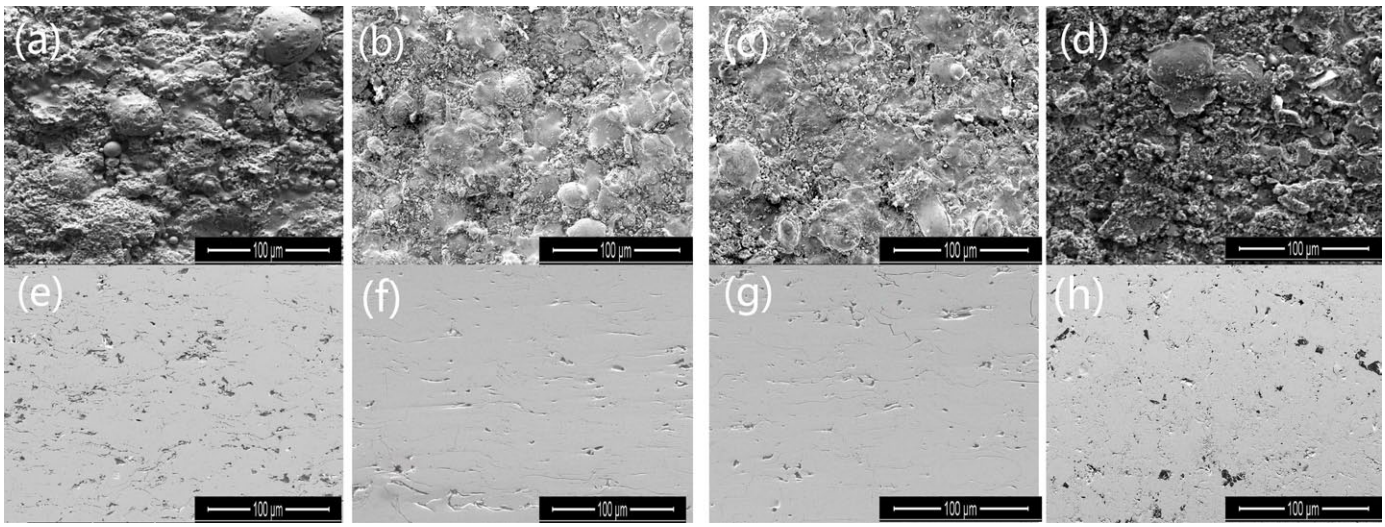


Fig. 12. SEM micrographs on the as-sprayed surface (a b c d) and cross-section (e f g h) show the general characteristics of the four HVAF coatings made from different barrel configurations (3E, 4L, 4E, 5L)

peaks associated with crystalline phases indicate that they are fully amorphous.

The structure of the cross-section and the surface morphology of different Ni-based AMs is shown in Fig. 12. The surface morphology reveals that barrel 3E was not fully melted during spraying (Fig. 12a). Thus the porosity of the coating for barrel configuration 3E is 5.06% (Fig. 12e), which is the highest than others. This is different from the coating with barrel configuration 4L and 4E, which were almost fully melted (see Fig. 12b,c). As we all known that the increase in particle velocity significantly improved the coating structure and density. So the porosity of the coating for barrel configuration 4E is lower than the coating for barrel configuration 4L. An almost fully dense coating with a porosity of approximately 2.09% was obtained for barrel configuration 4E (Fig. 12g) and a porosity of 2.57% was obtained for barrel configuration 4L (Fig. 12g). The surface morphology for the barrel 3E was excessive melted during spraying (Fig. 12d) and the porosity of the coating reached 4.03% (Fig. 12h). These results imply that the porosity of an HVAF coating is largely dependent on the barrel size and that the densest coating can be obtained by using barrel configuration (4E).

## 5. Conclusions

The influence of the barrel configurations on the porosity of a coating during HVAF thermal spray of Ni-based AM was studied using predictive simulations and verified via experiment. CFD is used to investigate the in-flight behavior of particles of Ni-based amorphous alloy powder in the HVAF spray process. For the gas-flow field, barrel size does not affect the initial chamber pressure. Increasing barrel diameter increases the variation of pressure at exit of barrel and these changes result in the severe fluctuation of flame velocity and temperature; the longer the length of barrel, the higher the flame velocity and temperature. And for the in-flight flow field, barrel length obviously affects the particle velocity and temperature, that is, the longer the length of barrel, the higher the particle velocity and temperature; barrel diameter has a slight influence on the particle velocity and temperature, that is, the larger the diameter of barrel, the higher the particle velocity and temperature. The barrel configurations (barrel diameter and barrel length) have a significant influence on both velocity and temperature of particles. The optimum thermal barrel configuration is 4E (230 mm, 14 mm) when the temperature of the powder is between the solidus and liquidus temperatures of Ni-based amorphous alloys. Using this optimized barrel configuration (4E), we obtained a low-porosity Ni-based AM.

**Acknowledgements**

This work was supported by Educational Commission of Liaoning Province of China under Grant No. L2020021; Fushun Revitalization Talents Program under Grant No. FSYC202107011.

## REFERENCES

[1] Z. Zhu, P. Jia, J. Xu, Scripta Mater. **64**, 785-788 (2011).
[2] A.P. Wang, X.C. Chang, W.L. Hou, Mater. Sci. Eng. A **449**, 277-280 (2007).
[3] A.P. Wang, T. Zhang, J.Q. Philos. Mag. Lett. **86**, 5-11 (2006).
[4] G. Huang, L. Qu, T. Lu, Vacuum. **153**, 39-42 (2018).
[5] L.D. Zhu, P.S. Xue, Q. Lan, G.R. Meng, Y. Ren, Z.C. Yang, P.H. Xu, Z. L, Optics and Laser Technology **138**, 106915 (2021).
[6] A.H. Dent, A.J. Horlock, D.G. McCartney, Surf. Coat. Technol. **139**, 244-250 (2001).
[7] H. Choi, S. Yoon, G. Kim, Scripta Mater. **53**, 125-130 (2005).
[8] Y. Wang, Z.Z. Xing, Q. Luo, Corros. Sci. **98**, 339-353 (2015).
[9] Q. Lei, Y.P. Wu, S. Hong, Surf. Coat. Technol. **366**, 296-302 (2019).

[10] N.C. Wu, K. Chen, W.H. Sun, Surf. Eng. **35**, 37-45 (2019).
[11] J. He, M. Ice, E. Lavernia, J. Therm. Spray Technol. **10**, 83-93 (2001).
[12] T.C. Hanson, G.S. Settles, J. Therm. Spray Technol. **12**, 403-415 (2003).
[13] V. Matikainen, H. Koivuluoto, P. Vuoristo, J. Therm. Spray Tech. **27**, 680-694 (2018).
[14] X. Gao, C. Li, D. Hang, J. Surf. Coat. Technol. **405**, 1265-1266 (2021).
[15] M.H. Lee, J.Y. Lee, D.H. Bae, Intermetallics. **12**, 1133-1137 (2004).
[16] H. Tabbara, S. Gu, Surf. Coat. Technol. **204**, 676-684 (2009).
[17] S. Kamnis, S. Gu, Chem. Eng. Process. **45**, 246-253 (2006).
[18] D. Cheng, Q. Xu, G. Tapaga, Part I: Gas phase dynamics, Metall. Mater. Trans. A **32**, 1609-1620 (2001).
[19] S. Gordon, B.J. McBride, (NASA Reference Publication 1311; Cleveland, OH: NASA), Cleveland. Ohio. USA. 1994.
[20] M.H. Khan, T. Shamim, Appl. Energy. **130**, 853-862 (2014).
[21] G. Montavon, C. Coddet, C.C. Berndt, J. Therm. Spray Technol. **7**, 229-241 (1998).
[22] H. Tabbara, S. Gu, J. Aiche. **11**, 3533-3544 (2012).
[23] R. Ghafouri-Azar, J. Mostaghimi, S. Chandra, J. Therm. Spray Technol. **12**, 53-69 (2003).
[24] J. Pan, S. Hu, L. Yang, Mater. **96**, 370-376 (2016).
[25] H.F. Voggenreiter, H. Huber, H.J. Spies, Materials Park (OH): ASM International 1997.